



Luminous Late-time Radio Emission from Supernovae Detected by the Karl G. Jansky Very Large Array Sky Survey (VLASS)

Michael C. Stroh¹, Giacomo Terreran^{1,13}, Deanne L. Coppejans¹, Joe S. Bright^{1,2}, Raffaella Margutti^{1,2}, Michael F. Bietenholz^{3,4}, Fabio De Colle⁵, Lindsay DeMarchi¹, Rodolfo Barniol Duran⁶, Danny Milisavljevic⁷, Kohta Murase^{8,9,10,11}, Kerry Paterson¹, and Wendy L. Williams¹²

¹ Center for Interdisciplinary Exploration and Research in Astrophysics (CIERA) and Department of Physics and Astronomy, Northwestern University, Evanston, IL 60201, USA; michael.stroh@northwestern.edu

² Department of Astronomy, University of California, Berkeley, CA 94720, USA

³ Department of Physics and Astronomy, York University, Toronto, M3J 1P3, ON, Canada

⁴ Hartebeesthoek Radio Observatory, P.O. Box 443, Krugersdorp, 1740, South Africa

⁵ Instituto de Ciencias Nucleares, Universidad Nacional Autónoma de México, A.P. 70-543 04510 D.F., Mexico

⁶ Department of Physics and Astronomy, California State University, Sacramento, 6000 J Street, Sacramento, CA 95819, USA

⁷ Department of Physics and Astronomy, Purdue University, 525 Northwestern Avenue, West Lafayette, IN 47907, USA

⁸ Department of Physics, The Pennsylvania State University, University Park, PA 16802, USA

⁹ Department of Astronomy & Astrophysics, The Pennsylvania State University, University Park, PA 16802, USA

¹⁰ Center for Multimessenger Astrophysics, Institute for Gravitation and the Cosmos, The Pennsylvania State University, University Park, PA 16802, USA

¹¹ Center for Gravitational Physics, Yukawa Institute for Theoretical Physics, Kyoto University, Sakyo-ku, Kyoto 606-8502, Japan

¹² Leiden Observatory, Leiden University, P.O. Box 9513, NL-2300 RA Leiden, The Netherlands

¹³ Las Cumbres Observatory, 6740 Cortona Drive, Suite 102, Goleta, CA 93117-5575, USA

Received 2021 June 17; revised 2021 November 3; accepted 2021 November 4; published 2021 December 16

Abstract


We present a population of 19 radio-luminous supernovae (SNe) with emission reaching $L_\nu \sim 10^{26} - 10^{29} \text{ erg s}^{-1} \text{ Hz}^{-1}$ in the first epoch of the Very Large Array Sky Survey (VLASS) at 2–4 GHz. Our sample includes one long gamma-ray burst, SN 2017iuk/GRB 171205A, and 18 core-collapse SNe detected at $\approx 1 - 60$ yr after explosion. No thermonuclear explosion shows evidence for bright radio emission, and hydrogen-poor progenitors dominate the subsample of core-collapse events with spectroscopic classification at the time of explosion (79%). We interpret these findings in the context of the expected radio emission from the forward shock interaction with the circumstellar medium (CSM). We conclude that these observations require a departure from the single wind-like density profile (i.e., $\rho_{\text{CSM}} \propto r^{-2}$) that is expected around massive stars and/or from a spherical Newtonian shock. Viable alternatives include the shock interaction with a detached, dense shell of CSM formed by a large effective progenitor mass-loss rate, $\dot{M} \sim 10^{-4} - 10^{-1} M_\odot \text{ yr}^{-1}$ (for an assumed wind velocity of 1000 km s^{-1}); emission from an off-axis relativistic jet entering our line of sight; or the emergence of emission from a newly born pulsar-wind nebula. The relativistic SN 2012ap that is detected 5.7 and 8.5 yr after explosion with $L_\nu \sim 10^{28} \text{ erg s}^{-1} \text{ Hz}^{-1}$ might constitute the first detections of an off-axis jet+cocoon system in a massive star. However, none of the VLASS SNe with archival data points are consistent with our model off-axis jet light curves. Future multiwavelength observations will distinguish among these scenarios. Our VLASS source catalogs, which were used to perform the VLASS cross-matching, are publicly available at <https://doi.org/10.5281/zenodo.4895112>.

Unified Astronomy Thesaurus concepts: Core-collapse supernovae (304); Radio transient sources (2008); Sky surveys (1464); Very Large Array (1766)

1. Introduction

Radio observations of stellar explosions in the years to decades after stellar demise constitute a probe of the physical properties of the fastest ejecta in the explosion (i.e., their velocity and energy) and the environment at large distances of $r \geq 10^{17} \text{ cm}$ (i.e., the density of the circumstellar medium, CSM), e.g., Chevalier & Fransson (2017). There are three main sources of bright nonthermal synchrotron radio emission in supernovae (SNe) at $t \geq 1$ yr: (i) the deceleration of the forward shock in a dense environment (e.g., Chevalier 1998; Chevalier & Fransson 2006), (ii) emission from an off-axis relativistic jet entering our line of sight (e.g., Granot et al. 2002), and (iii) emergence of emission from a newly formed pulsar-wind nebula

(PWN; Slane 2017). Late-time radio observations of cosmic explosions can thus reveal a complex mass-loss history of the stellar progenitors in the years leading up to core collapse, jet-driven explosions similar to long gamma-ray bursts (GRBs) that launched a jet that was misaligned with our line of sight, or the energetics and properties of the compact object remnant. However, most SNe are not observed at radio wavelengths at very late times. For example, in the sample of 294 SNe observed at $\sim 5 - 8$ GHz compiled by Bietenholz et al. (2021), only 87 were observed at more than 1000 days postexplosion, and of these, only 28 were detected.¹⁴ As a result, the late-time radio emission from SNe constitutes a poorly explored region of the phase space (Figure 2 in Bietenholz et al. 2021).

 Original content from this work may be used under the terms of the [Creative Commons Attribution 4.0 licence](https://creativecommons.org/licenses/by/4.0/). Any further distribution of this work must maintain attribution to the author(s) and the title of the work, journal citation and DOI.

¹⁴ This sample is one of the largest compilations of radio observations of SNe. We note that it is not a complete sample (see Bietenholz et al. 2021), so these numbers are likely underestimates. One important selection effect is that the peak frequency of the radio emission from SNe declines with time, so lower-frequency observations would yield a higher detection rate.

Here we present a sample of 19 radio-luminous SNe detected in the first epoch of the Very Large Array Sky Survey (VLASS; Lacy et al. 2020) carried out by the Karl G. Jansky Very Large Array (VLA). VLASS is a successor and complementary survey to the National Radio Astronomy Observatory (NRAO) VLA Sky Survey (NVSS; Condon et al. 1998) and Faint Images of the Radio Sky at Twenty cm (FIRST; Becker et al. 1995) survey. The survey is conducted at 2–4 GHz and split into three distinct epochs, each scanning the full survey region (decl. $\delta > -40^\circ$) with an ≈ 32 month observing cadence reaching an rms noise of $120 \mu\text{Jy beam}^{-1} \text{ epoch}^{-1}$. Lacy et al. (2020) note “Hidden Explosions and Transient Events” as a key VLASS science theme, and Hallinan et al. (2020) demonstrated the synergy between VLASS and newly discovered transients with the detection of the Type II SN 2019xhb in the second VLASS observing epoch 202 days after discovery. Importantly, by scanning the northern sky, VLASS offers the opportunity to perform a systematic and unbiased survey of the late-time radio emission from the tens of thousands of previously reported SNe. With the exception of SN 2017iuk/GRB 171205A, the sample of radio-luminous SNe presented in this paper was imaged at an epoch corresponding to ≈ 1 –60 yr postexplosion.

This paper is organized as follows. In Section 2, we describe our methodology for identifying optically detected SNe in the VLASS sample, explain how we filtered out potential spurious detections, and present our list of VLASS-detected SNe. Section 3 discusses the physical processes that could produce the bright radio emission associated with the SNe. Finally, in Section 4, we summarize the conclusions.

2. A Sample of SNe with Luminous Late-time Radio Emission

We created a catalog consisting of all publicly announced optical SNe by combining the Bright Supernovae,¹⁵ Open SNe,¹⁶ and Transient Name Server¹⁷ catalogs. We included all optical SNe detected prior to 2020 January 1, leading to an initial sample of $\approx 70,000$ unique SNe. Two independently generated VLASS detection catalogs were produced using the $\approx 35,000$ VLASS epoch 1 quick-look images provided by NRAO.

2.1. PyBDSF Detections

The complete VLASS epoch 1 was processed using the Python Blob Detector and Source Finder version 1.9.1 (PyBDSF; Mohan & Rafferty 2015). We created a local catalog consisting of all detections using a source detection threshold of 5σ ($\text{thresh_pix}=5.0$) and a threshold for islands of 3σ ($\text{thresh_isl}=3.0$) and fixing the source components to be Gaussian with major axis, minor axis, and position angle equal to the synthesized beam shape from the respective VLASS observations ($\text{fix_to_beam}=\text{True}$). The values of thresh_pix and thresh_isl are used to calculate pixel islands of significant emission. The thresh_pix parameter is used to identify significant pixels (where the pixel value is greater than $\text{mean} + \text{thresh_pix} \times \sigma$, where σ is the rms noise of the image) used for fitting, with the mean map calculated using a box of pixel size and pixel step size

either calculated within PyBDSF or set manually by the user. The fitting region is then extended based on the value of thresh_isl such that all pixels greater than $\text{mean} + \text{thresh_isl} \times \sigma$ that are adjacent (including diagonally) to a significant pixel identified using thresh_pix are included in the fitting region or “island” (if this process causes islands to overlap, they are combined). Multiple Gaussians are then fit to the island in order to best describe the source (the collection of Gaussians within an island), and we fixed the Gaussians to the shape of the synthesized beam.

This VLASS-PyBDSF catalog resulted in 3,752,214 sources, similar to the 3,381,277 VLASS sources cataloged by the Canadian Initiative for Radio Astronomy Data Analysis (CIRADA; Gordon et al. 2020), and more than the 2,232,726 sources in the VLASS Quicklook Catalog (Bruzewski et al. 2021). Our VLASS-PyBDSF catalog is publicly available at [10.5281/zenodo.4895112](https://zenodo.org/record/4895112).

2.2. SExtractor Detections

We created an initial list of possible VLASS source detections using SExtractor version 2.25.0 (Bertin & Arnouts 1996). SExtractor is not optimized for radio imaging analysis, but through trial and error with fields where transients were known to exist, we settled on a requirement of at least 5 contiguous pixels (detect_minarea) to be above the low $\text{detect_threshold}=5\sigma$. The VLASS-SExtractor catalog contained 9,652,665 possible source detections. Most of these detections are likely spurious, as evidenced by the number of sources detected by the previous section. We note that SExtractor runs at least an order of magnitude faster through VLASS quick-look images than PyBDSF, so it may be preferred for studies where a large number of possible bogus detections are acceptable. Our VLASS-SExtractor catalog is publicly available at [10.5281/zenodo.4895112](https://zenodo.org/record/4895112).

2.3. Identifying SNe for Cross-matching

We chose low detection thresholds in order to minimize the chance that we may miss potential SN cross-matches on our initial pass. In order to reduce the number of spurious matches, we required the potential SN cross-matches to be detected by both the VLASS-SExtractor and VLASS-PyBDSF catalogs. We cross-matched the locations of the optical SNe with the VLASS-PyBDSF and VLASS-SExtractor catalogs using a $5''$ angular separation. This separation is \approx twice the average VLASS beam size and helps account for a lack of positional precision in SN discovery reports. Using our initial list of $\approx 70,000$ SNe, ≈ 1600 and ≈ 1400 SNe have potential PyBDSF and SExtractor cross-matches, respectively. By requiring that a source must have cross-matches in both the VLASS-PyBDSF and VLASS-SExtractor catalogs, we have ≈ 1300 potential cross-matches in VLASS. We further required the VLASS observation to have occurred after the SN discovery date.

The possible VLASS SNe were visually inspected to ensure that the VLASS SN detections are real and not due to radio imaging artifacts (see, for example, Figure 1). We also rejected SNe when the location of the radio source broadly overlapped with that of the galactic nucleus. After visual inspection, only ≈ 100 potential VLASS SN detections remained.

¹⁵ <http://rochesterastronomy.org/snimages>

¹⁶ <https://sne.space>

¹⁷ <https://www.wis-tns.org>

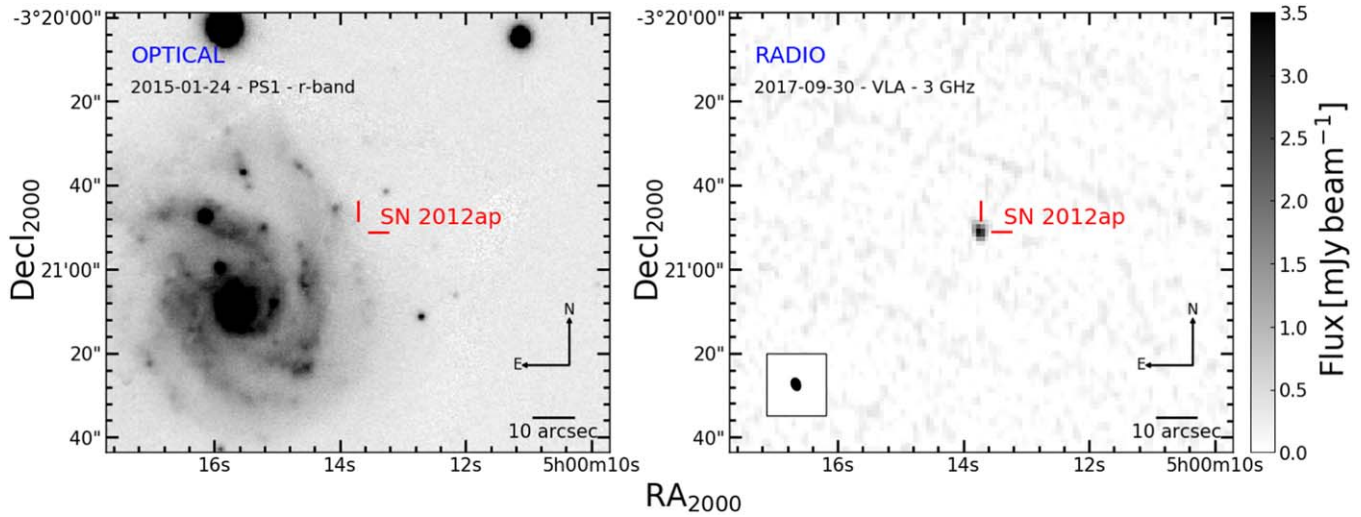


Figure 1. Field of SN 2012ap in the Pan-STARRS1 r band (left) and at 3 GHz with VLASS (right). The red lines indicate the optical SN position, and each image notes the date of each observation. The optical image clearly shows the host galaxy of SN 2012ap, but no emission from the host is found in the optical image near the optical SN position. No radio emission is found in the field near SN 2012ap except near the optical SN position. The VLASS image was taken 2065 days after explosion (Milisavljevic et al. 2014).

2.4. Multiwavelength Cross-matching

In order to filter out known radio sources, we rejected associations that had counterparts in the NVSS or FIRST catalogs prior to their explosion date. We removed VLASS SNe near active galactic nuclei (AGNs) identified by Assef et al. (2018), who cataloged probable AGNs in the Wide-field Infrared Survey Explorer (WISE; Wright et al. 2010) AllWISE data release (Cutri et al. 2013).

D’Abrusco et al. (2013) examined the chance of probability for spurious associations between a sample of NVSS-detected blazars and AllWISE. They calculated the number of additional cross-matches between their NVSS blazar catalog and AllWISE ΔN_r as the cross-matching radius increased. Similarly, the number of additional spurious cross-matches per increasing cross-matching radius, ΔN_r , was calculated by adding a random offset to the NVSS blazar positions. D’Abrusco et al. (2013) found that $\Delta N_r > \Delta N_r$ for cross-matching radii above $3''3$; thus, a cross-matching radius of $3''3$ can be considered a cross-match between pointlike VLA sources and AllWISE. For the infrared AGN cross-matching, we adopted the $3''3$ angular search radius suggested by D’Abrusco et al. (2013).

Possibly misidentified AGNs were also removed by cross-matching our VLASS SN candidates against the Chandra Source Catalog v2.0 (CSC 2.0; Evans et al. 2020a), the most recent XMM-Newton X-ray source data release (4XMM-DR10; Webb et al. 2020), and the second Swift-XRT point-source catalog (2SXPS; Evans et al. 2020b). The error in the X-ray position is generally greater than the astrometric uncertainties in the VLASS positions (see the Appendix of Bruzewski et al. 2021); thus, for X-ray catalog cross-matching, we removed sources within the 1σ X-ray error region in the respective X-ray catalog. We ensured that no VLASS SN candidates were rejected by targeted SN follow-up observations.

We further inspected the VLASS SN candidates within the 424 deg^2 covered so far by the LOFAR Two-meter Sky Survey (LoTSS Data Release 1; Shimwell et al. 2019) to ensure that

none were classified as AGNs based on their 150 MHz radio morphology or luminosity or multiwavelength cross-identifications (Williams et al. 2019). While only two of the candidates lie within this area, both were detected as star-forming galaxies. Further releases of LoTSS over the northern sky will enable further such comparisons.

This multiwavelength filtering procedure leads to a sample of 19 core-collapse SNe with associated VLASS emission. The final VLASS SN sample is listed in Table 1. All VLASS SNe also have counterparts in the CIRADA VLASS catalog, and SN 2017hcb is the only source without a cross-match in the VLASS Quicklook Catalog. Interestingly, we note that no thermonuclear explosion (i.e., Ia-like) passed the criteria above, in spite of it largely dominating the initial optical SN sample. The lack of Type Ia SNe in the sample is consistent with the lack of radio emission associated with Type Ia (e.g., Chomiuk et al. 2016), but the lack chance coincidence matches may be evidence of the strength of our multiwavelength filtering described above. Of the 14 VLASS-detected SNe with early-time spectroscopic classification, 13 (93%) and 12 (86%) are detected at $>10^2$ and $>10^3$ days postexplosion, respectively. The SNe with hydrogen-poor progenitors at the time of explosion make up the majority 11 (79%) of the sources with early-time spectroscopic classification. Remarkably, we find that SN 2012ap, one of the only two known SNe with relativistic ejecta without a GRB (Margutti et al. 2014a; Chakraborti et al. 2015; Milisavljevic et al. 2015a), shows evidence for bright radio emission years after explosion and is a member of the sample. The very nearby SN 2017iuk/GRB 171205A, at redshift $z = 0.0368$ (de Ugarte Postigo et al. 2017), was detected in the first VLASS epoch less than 60 days following the Swift trigger.

2.5. Final Flux Densities

In addition to a complete and consistent processing of VLASS epoch 1 (as described in Section 2.1), we performed an optimized manual analysis on each of the fields containing the sources listed in Table 1. The default significance parameters

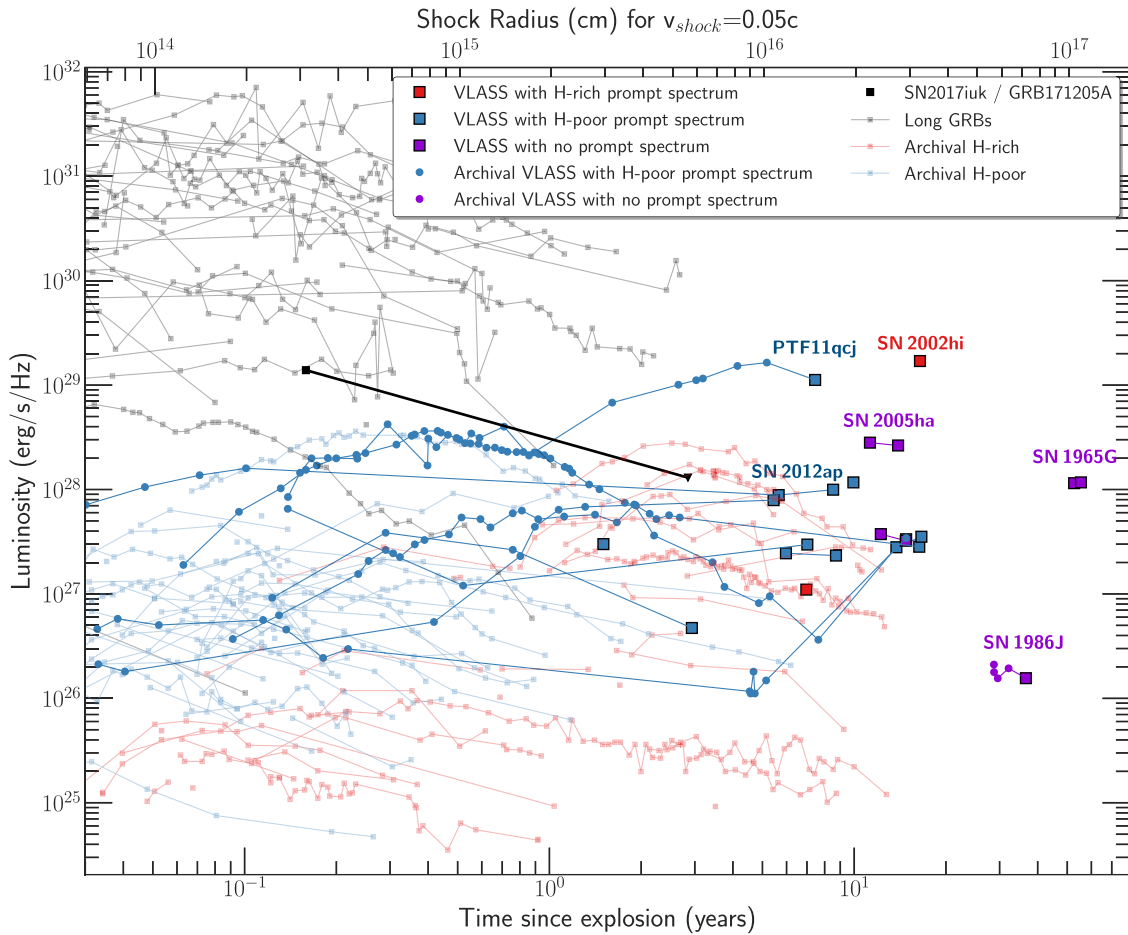


Figure 2. VLASS SNe detections in the context of H-rich SNe (red), H-poor SNe (blue) SNe, and long GRBs (gray). A number of the VLASS observations were taken at a later stage than SNe are typically observed and detected at radio wavelengths and show brighter emission than would be expected at this epoch. Notably, the H-poor VLASS SNe were observed years after the radio emission (at ≥ 1 GHz) from this class typically fades. Archival radio light curves for VLASS-detected SNe are included: SN 1986J (3–5 GHz; Bietenholz & Bartel 2017), SN 2003bg (4.86 GHz; Soderberg et al. 2006a), SN 2004C (4.9 GHz; L. DeMarchi 2021, in preparation), SN 2004dk (3–5 GHz; Wellons et al. 2012; Balasubramanian et al. 2021), PTF 11qej (3–4 GHz; Corsi et al. 2014; Palliyaguru et al. 2019), SN 2012ap (3 GHz extrapolation based on radio SED modeling; Chakraborti et al. 2015), SN 2012au (3–4 GHz; Kamble et al. 2014; G. Terreran et al. 2021, in preparation), SN 2014C (7.1 GHz; Margutti et al. 2017), and SN 2016coi (3 GHz; Terreran et al. 2019). The archival radio observations of SNe are from Bietenholz et al. (2021), and the archival long GRBs are from Chandra & Frail (2012). Most archival historical light curves are at 8.6 GHz, as the 3 GHz light curves are not well sampled. From the VLASS-detected sample, SDSS-II SN 8524 is not included, since its host galaxy and redshift are unknown; thus, a luminosity cannot be calculated. The H-rich and H-poor designations are inferred from the spectrum near the time of explosion. The upper x-axis provides a reference distance scale for a fiducial normal SN shock velocity of $0.05c$ with no deceleration. This figure highlights the presence of two groups of H-rich SNe in the radio phase space, with IIc SNe belonging to the group with luminous radio emission years after explosion (see, e.g., Bietenholz et al. 2021).

used for this analysis were `thresh_isl=5.0` and `thresh_pix=5.0`, with an adaptive region used to calculate the rms and mean maps (`adaptive_rms_box=True`) and components fixed to be the same shape as the synthesized beam (`fix_to_beam=True`). The island and pixel threshold values were adjusted on a per-field basis depending on, e.g., bright source artifacts or extended host structure; however, we require `thresh_pix \geq thresh_isl`. Adaptive rms calculation ensures that the region size near bright sources is reduced compared to regions devoid of bright emission, properly accounting for elevated rms levels resulting from imaging artifacts (an issue in a number of the VLASS fields). For fields with particularly strong artifacts, we set the rms box and step sizes manually such that the noise map captured the variation caused by the artifacts. In the cases where the SN emission formed part of an extended emission complex from the host galaxy, we set `fix_to_beam=False` in order to better model the emitting region. We ran PyBDSF in interactive mode (`interactive=True`) and manually inspected the result of the island and

source detection, adjusting our significance threshold and the size of the region used to calculate the rms noise to improve the source fitting.

For fields with extreme imaging artifacts around bright sources, we manually set the rms box size and disabled adaptive region sizing. In a handful of cases, emission from the transient was part of a larger emission complex (radio emission from the host galaxies), and the emission island was better described using Gaussians with unconstrained shapes. We list the results of our fitting in Table 1 and note any deviations from the default parameters. Additionally, we analyze each of the target fields and list the flux densities and position of the sources in the first half of the second VLASS epoch (i.e., epoch 2.1). In the cases of SN 2017iuk/GRB 171205A and SDSS-II SN 8524, the source is no longer detected in the second epoch, so instead, we list a 3σ upper limit. We compare the luminosities and timescales of the VLASS-detected SNe to historical radio light curves in Figure 2.

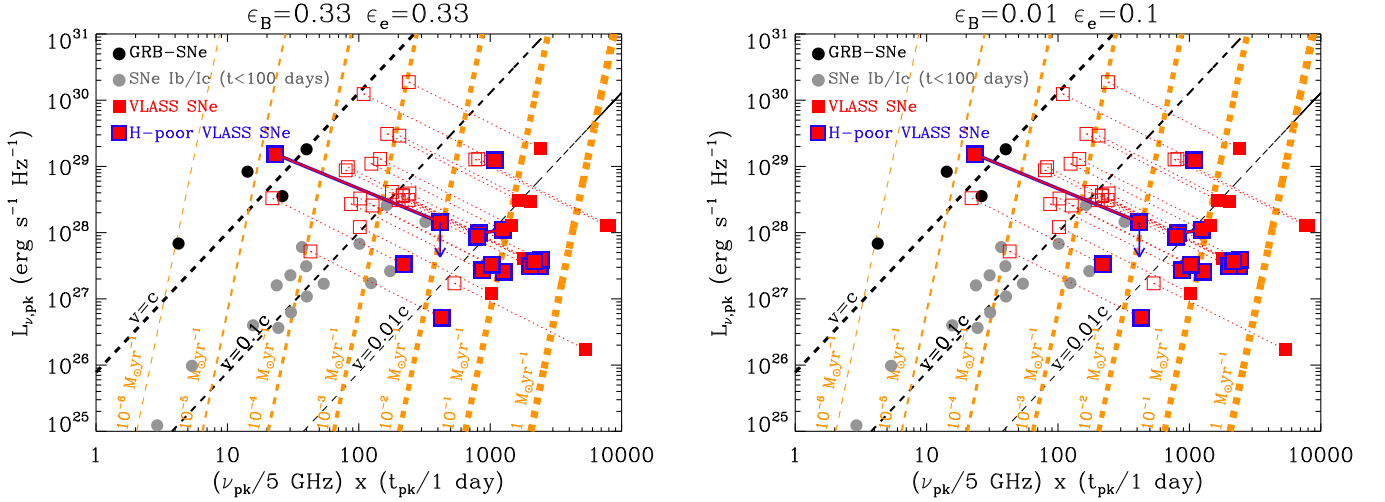


Figure 3. Location of the VLASS SNe (red filled squares) in the phase space of radio observables. A blue outline marks the VLASS SNe with an H-poor spectrum at the time of explosion. Black filled circles: GRB SNe. Gray filled circles: H-stripped SNe from radio observations typically acquired at $\lesssim 100$ days since explosion. We assume $p = 3$ and the shock microphysics indicated in the title of each plot. Black dashed lines: lines of constant shock velocity assuming SSA only. Orange dashed lines: lines of constant mass-loss rate, here calculated for an assumed wind velocity of 10^3 km s^{-1} . The red filled squares show what the properties of the VLASS SNe would be in the case where the emission peaked in the VLASS band at the time of the observations (see Section 3.1). Red open squares: location of the VLASS SNe for an optically thin spectrum $L_\nu \propto \nu^{-1}$, assuming that the ν_{pk} of the SSA spectrum is below the VLASS band at $\approx 0.3 \text{ GHz}$. The VLASS object that crosses the $v = c$ line is SN 2017iuk/GRB 171205A. VLASS Memo 13 reported an $\sim 10\%$ overestimate in flux densities from the VLASS epoch 1 quick-look data. No appreciable difference is found in this analysis when applying a 10% correction to these figures. References: Soderberg et al. (2012) and references therein.

3. Powering Luminous Late-time Radio Emission

Winds from massive stars enhance and shape the density of their immediate surroundings (e.g., Smith 2014). Radio emission from stellar explosions is normally associated with an interaction between the fastest SN ejecta (i.e., the blast wave) and the wind-shaped CSM. As the forward shock propagates through the CSM, the electrons are accelerated, creating a bell-shaped nonthermal synchrotron spectrum (Chevalier & Fransson 2017). The radio spectrum is characterized by a peak frequency, ν_{pk} , that cascades to lower frequencies as the blast wave expands (e.g., Chevalier 1998; Chevalier & Fransson 2006). For synchrotron self-absorption (SSA)-dominated spectra, Chevalier (1998) suggested $\nu_{\text{pk}} \propto R^{2/7} B^{9/7}$, and the spectral peak flux $F_{\text{pk}} \propto R^{19/7} B^{19/7}$, where R is the forward shock radius and B is the postshock magnetic field. The optically thin flux density at $\nu > \nu_{\text{pk}}$ scales as $F_{\nu,\text{thin}} \propto \nu^{-(p-1)/2}$ (where p is the power-law index of the electron distribution, $N_e(\gamma_e) \propto \gamma_e^{-p}$, and γ_e is the electron Lorentz factor), and the optically thick spectrum at $\nu < \nu_{\text{pk}}$ is described as $F_{\nu,\text{thick}} \propto \nu^{5/2}$.

During the SN interaction phase with a “wind density profile” environment expected around massive stars ($\rho_{\text{CSM}} \propto r^{-2}$), the self-similar solutions by Chevalier (1982) apply, and the shock radius evolves with time as $R \propto t^{\frac{n-3}{n-2}}$, where the density in the outer layers of the stellar progenitor has been parameterized as $\rho_{\text{SN}} \propto r^{-n}$. In the limit of no evolution of the shock microphysical parameters (e.g., the fraction of postshock energy in magnetic fields and relativistic electrons, ϵ_B and ϵ_e) and using $n \approx 10$ as appropriate for compact massive stars (Matzner & McKee 1999; Chevalier & Fransson 2006), the equations above imply $\nu_{\text{pk}} \approx t^{-1}$ and $F_{\text{pk}} \approx \text{constant}$. Since radio SNe typically show $p \approx 3$ (or $F_{\nu,\text{thin}} \propto \nu^{-1}$), $L_{\nu,\text{pk}} \leq 10^{28} \text{ erg s}^{-1} \text{ Hz}^{-1}$, and $\nu_{\text{pk}} \leq 10 \text{ GHz}$ at $< 0.1 \text{ yr}$ after explosion, the prediction of this single-wind model is $\nu_{\text{pk}} \ll 1 \text{ GHz}$ and a luminosity of $< 10^{27} \text{ erg s}^{-1} \text{ Hz}^{-1}$ in the VLASS bandpass at the current epoch (which

corresponds to $> 10^3$ days since explosion; Figure 2). We conclude that our sample of VLASS SNe requires a deviation from a single-wind model.

In the remainder of this section, we discuss three alternative explanations: (i) interaction of the SN shock with dense shells of CSM (Section 3.1), (ii) emission from an off-axis relativistic jet entering our line of sight (Section 3.2), and (iii) emergence of emission from a PWN (Section 3.3).

3.1. Dense Detached CSM Shells in the Local SN Environment

VLASS SNe show a level of radio emission comparable to the most luminous Type IIIn SNe (Figure 2). We place the VLASS SNe into the phase space of radio observables ν_{pk} , $L_{\nu,\text{pk}}$, and peak time t_{pk} in Figure 3, where we calculate lines of constant shock velocity v_{sh} and mass-loss rate \dot{M} following the standard formulation of SSA radio emission from a blast wave during the interaction phase with a wind-like environment (e.g., Chevalier 1998; Soderberg et al. 2005; Chevalier & Fransson 2006; Soderberg et al. 2012). Equipartition of energy between the relativistic electrons, protons, and magnetic field, i.e., $\epsilon_e = \epsilon_B = 1/3$, where ϵ_e is the fraction of thermal energy stored in electrons, and ϵ_B is the fraction of magnetic energy relative to the thermal energy, leads to a solid lower limit on the mass-loss rate parameter \dot{M} for a given wind velocity (v_w), where $\rho_{\text{CSM}} = \frac{\dot{M}}{4\pi v_w r^2}$. We present our results for both $\epsilon_e = \epsilon_B = 1/3$ and $\epsilon_e = 0.1$ and $\epsilon_B = 0.01$. Our discussion below focuses on our fiducial case of $\epsilon_e = 0.1$ and $\epsilon_B = 0.01$. All \dot{M} values quoted are for a wind velocity $v_w = 10^3 \text{ km s}^{-1}$. A few considerations follow from Figure 3.

1. If $\nu_{\text{pk}} \gtrsim \nu_{\text{obs}}$ (where ν_{obs} is the frequency of the VLASS observations), then VLASS SNe require very dense environments with an effective $\dot{M} \gtrsim 0.1 M_\odot \text{ yr}^{-1}$, which is significantly larger than the typical \dot{M} inferred for non-Type IIIn SN progenitors that comprise the majority of our sample (Smith 2014). In absolute terms, the inferred \dot{M} would

compete with the most extreme mass-loss rates invoked for evolved massive stars.

2. A lower $\nu_{\text{pk}} < \nu_{\text{obs}}$ would bring the VLASS SNe in line with the lower $\dot{M} \sim 10^{-4}\text{--}10^{-3} M_{\odot} \text{ yr}^{-1}$ that is typical of massive stars. The open squares of Figure 3 show the location of VLASS SNe for $\nu_{\text{pk}} = 0.3 \text{ GHz}$ as an example. However, the lower ν_{pk} would also lead to shock velocities $v_{\text{sh}} \geq 0.1c$ and $L_{\nu_{\text{pk}}} > 10^{28} \text{ erg s}^{-1} \text{ Hz}^{-1}$, implying that VLASS SNe would constitute a class of radio SNe as luminous as long GRBs and with mildly relativistic shocks at $>10^3$ days (and likely faster at earlier times).

Since earlier-time radio follow-up of some VLASS SNe indicated “normal” SN shock speeds of $\sim 0.1\text{--}0.2c$ at a few months postexplosion (e.g., SN 2012au in Kamble et al. 2014), it is clear that the relativistic ejecta scenario cannot explain the entire VLASS SN sample unless the relativistic ejecta is highly collimated (i.e., a jet) and pointing away from our line of sight at early times (i.e., off-axis). We further explore the relativistic ejecta scenario in Section 3.2.

Mass-loss rates $\dot{M} \gtrsim 0.1 M_{\odot} \text{ yr}^{-1}$, if sustained until the time of explosion, would lead to very prominent Type II_n-like spectroscopic features at earlier times for all VLASS SNe, which were not observed for the majority of the sample. Earlier radio observations of some targets also pointed to significantly lower $\dot{M} \approx 10^{-5} M_{\odot} \text{ yr}^{-1}$ (e.g., SNe 2004dk, 2012au, and 2012ap; Wellons et al. 2012; Kamble et al. 2014; Chakraborti et al. 2015) at the smaller radii probed at those epochs, $r \lesssim 5 \times 10^{16} \text{ cm}$. The emerging picture is that at least some VLASS SNe exploded in a low-density bubble surrounded by a shell of dense material at $r \sim v_{\text{sh}} \delta t = (v_{\text{sh}}/10^4 \text{ km s}^{-1})(\delta t/8000 \text{ days}) \approx 0.5 \text{ pc}$, consistent with the findings from the multiwavelength monitoring of SNe 2003bg, 2004C, 2004dk, and 2014C and PTF 11qcj (Soderberg et al. 2006a; Corsi et al. 2014; Margutti et al. 2017; Murase et al. 2019; Palliyaguru et al. 2019; Pooley et al. 2019; Brethauer et al. 2020; Balasubramanian et al. 2021, L. DeMarchi 2021, in preparation). For VLASS SNe from H-poor stellar progenitors (which, interestingly, dominate the sample), these overdensities might represent the shedding of their H-rich envelope in the centuries before core collapse. Optical spectroscopy at the time of the radio rebrightenings of SN 2003bg, SN 2004dk, SN 2014C, and PTF 11qcj confirmed the later appearance of H features in the spectra (Soderberg et al. 2006a; Milisavljevic et al. 2015b; Palliyaguru et al. 2019; Pooley et al. 2019), consistent with this scenario.

Potential theoretical explanations of this phenomenology include the interaction of faster Wolf-Rayet winds with the slower winds of the red supergiant phase coupled with a shorter-than-expected Wolf-Rayet phase, envelope ejection due to binary interaction, or mass shedding due to gravity wave-powered mass loss (e.g., Smith 2014; Zhao & Fuller 2020; Wu & Fuller 2021).

3.2. Off-axis Relativistic Jets

Off-axis jets can result in bright synchrotron emission that peaks years after explosion (e.g., Granot et al. 2002, 2018). The emission from off-axis jets enters our line of sight as the jet decelerates in the ambient medium and relativistic beaming becomes less severe (Rhoads 1997; Sari et al. 1999). The fraction of stellar explosions that are jet-driven is still unclear (e.g., Soderberg et al. 2006b; Bietenholz et al. 2014; Corsi et al. 2016;

Corsi & Lazzati 2021). Successful relativistic jets have so far been associated with broad-line Type Ic SNe accompanying cosmological GRBs, while partially successful and partially failed jets have been proposed to be powering low-luminosity GRBs and relativistic SNe, respectively (e.g., for observations, see Margutti et al. 2014a; for theory, see Morsony et al. 2007; Lazzati et al. 2012). While observations of energetic H-stripped SNe point to a continuum of jet properties from normal Ibc SNe to GRB SNe (e.g., Mazzali et al. 2008; Xu & Wei 2008; Margutti et al. 2014b; Corsi & Lazzati 2021), no bona fide off-axis jet has ever been associated with an SN without a GRB detection. In this context, it is particularly interesting to note that the relativistic SN 2012ap, which is one of only two known relativistic SNe without a GRB counterpart (Soderberg et al. 2010; Chakraborti et al. 2015), is detected by VLASS observations 5.7 and 8.5 yr after explosion. Thus, SN 2012ap is a clear candidate for an off-axis jet driving late-time emission.

To determine whether the detected VLASS emission is associated with off-axis jets, we generated a set of synthetic 3 GHz jet afterglow light curves with Boxfit v2 (van Eerten et al. 2012). Boxfit assumes a top-hat jet structure, i.e., a jet with energy uniformly distributed within $\theta \leq \theta_{\text{jet}}$ and $E = 0$ for $\theta > \theta_{\text{jet}}$. We assumed a wind-like CSM density profile. We explored the parameter space with a grid of parameter values defined as follows: isotropic-equivalent jet kinetic energies of $E_{\text{iso}} = [10^{50}, 10^{51}, 10^{52}, 10^{53}, 10^{54}, 10^{55}] \text{ erg}$, jet opening angles of $\theta_{\text{jet}} = [5^{\circ}, 15^{\circ}, 30^{\circ}]$, off-axis angle $\theta_{\text{obs}} = [30^{\circ}, 60^{\circ}, 90^{\circ}]$ from our line of sight, mass-loss rates of $\dot{M} = [10^{-8}, 10^{-7}, 10^{-6}, 10^{-5}, 10^{-4}, 10^{-3}] M_{\odot} \text{ yr}^{-1}$ for $v_w = 1000 \text{ km s}^{-1}$, and shock microphysical parameters $\epsilon_e = 0.1$, $\epsilon_B = [0.001, 0.01]$, and $p = [2, 2.5, 3]$. Finally, we used the χ^2 as a metric to evaluate the agreement between the models and the VLASS data of Figure 2.

None of the VLASS SNe with archival (i.e., pre-VLASS) data points are consistent with our model off-axis jet light curves. We find that the synthetic models that best approximate the VLASS data of SDSS-II SN 12882, SN 2002hi, SN 2005 ha, SN 2009fi, and SN 2012cc with $\chi^2 \lesssim 1$ have large off-axis angles $\theta_{\text{obs}} \geq 60^{\circ}$, large densities corresponding to $\dot{M} > 10^{-5} M_{\odot} \text{ yr}^{-1}$, $p \sim 3$, $\epsilon_B = 0.01$ coupled with large $E_{\text{iso}} \geq 10^{54} \text{ erg}$, and large jet angles $\theta_{\text{jet}} \geq 15^{\circ}$. The values of these parameters are driven by the large radio luminosities of the sample at late times and imply extremely large beaming-corrected jet energies of $3 \times 10^{52}\text{--}10^{54} \text{ erg}$. While we show some examples of top-hat off-axis jet light curves consistent with the VLASS data in Figure 4, we consider this top-hat jet scenario unlikely because of the large jet energies needed and the fact that only SNe with a sparse data set can be fitted. We consider alternative jet models and environments below.

We start by noting that in SN 1965G, SN 2004C, SN 2005 ha, SN 2012ap, SN 2012at, and SDSS-II SN 12882, the radio flux density remains nearly constant over $\sim 2\text{--}3$ yr between two VLASS epochs. Object SN 1986J also has nearly constant radio flux densities (see Figure 2); however, it has only been observed in a single VLASS epoch. Numerical simulations of GRB jets propagating through a stratified medium show that nearly flat, wide peaks are obtained only if the jet propagates through a wind-profile medium with $\rho \propto r^{-2}$ (see Figure 1 in Granot et al. 2018). Jets propagating through a uniform density environment have a much narrower peak (e.g., as seen in the GRB 170817A afterglow; Margutti & Chornock 2021) and are ruled out by our observations. Object GRB 170817A also clearly showed that relativistic jets can

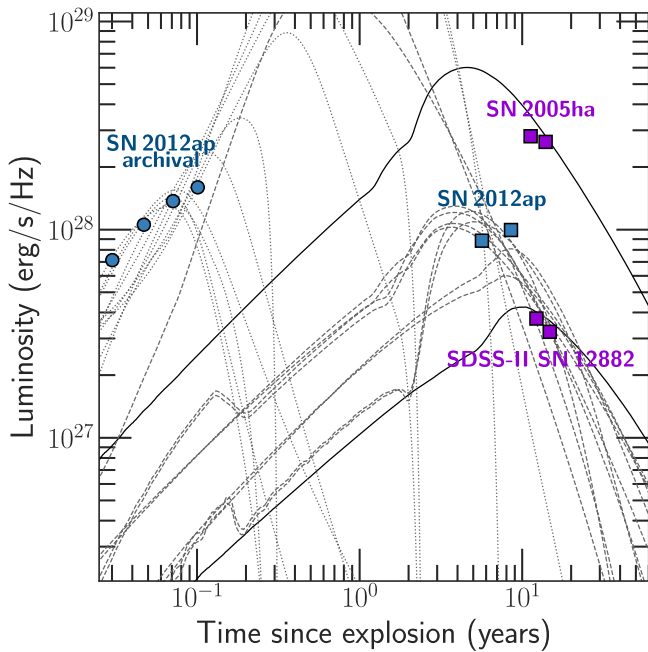


Figure 4. VLASS SN 3 GHz light curves for SN 2005 ha, SN 2012ap, and SDSS-II SN 12882. The 3 GHz SN 2012ap archival light curve is included using the model from Chakraborti et al. (2015). The SN 2012ap light curve is shown along with the 10 top-hat jet models in our grid that best fit the VLASS-only light curve (gray dashed lines) and the 10 models that best fit the combined VLASS and archival light curve (gray dotted lines). Objects SN 2005 ha and SDSS-II SN 12882 are the only multiphase detected VLASS SNe that are consistent with off-axis jet models from our grid (i.e., $\chi^2 < 1$). The solid black lines represent the off-axis jet models that are consistent with SN 2005 ha and SDSS-II SN 12882 light curves. Objects SN 2005 ha and SDSS-II SN 12882 had limited spectroscopic follow-up and were not classified as H-rich or H-poor (e.g., Marsden 2005). We show this figure as a proof of concept, but we note that the models that best fit the SN 2005 ha and SDSS-II SN 12882 light curves have high isotropic kinetic energies of $E_{\text{iso}} = 10^{55}$ erg, corresponding to beaming-corrected energies of $E = 3 \times 10^{53}$ and 1×10^{54} erg for SN 2005 ha and SDSS-II SN 12882, respectively, and are likely unrealistic.

have angular structure (i.e., the jet is not necessarily top-hat; see, e.g., Nakar 2020 and references therein).

The propagation of relativistic GRB jets through a massive Wolf-Rayet progenitor star leads to the production of extended wide-angle outflows known as cocoons, with masses of $\approx 10^{-2}$ – $10^{-1} M_{\odot}$ and energies $\approx 10^{50}$ – 10^{51} ergs (see, e.g., Lazzati & Begelman 2005; Nakar & Piran 2017; De Colle et al. 2021), possibly observationally identified in SN 2017iuk/GRB 171205A (Izzo et al. 2019). Once the jet breaks out of the star, the cocoon engulfs the star and expands nearly spherically into the environment (see, e.g., Figure 3 of De Colle et al. 2021). The cocoon initially expands with relativistic velocities (corresponding to Lorentz factors of ~ 2 – 10) but later decelerates to mildly relativistic velocities at $\sim 10^{16}$ cm (see Figure 2 in De Colle et al. 2018). Particle acceleration through the shock cocoon itself will lead to a bright afterglow. While GRB jets are collimated and enter into the observer line of sight only at late times, the cocoon radio emission should be detectable at early times by observers located at nearly all angles (as beaming effects are much less important in the slower-moving cocoon material) and would thus be able to explain the larger radio fluxes of pre-VLASS observations. The predicted early-time radio emission (De Colle et al. 2018, 2021) is similar to that observed in relativistic SNe 2009bb and 2012ap (Soderberg et al. 2010;

Margutti et al. 2014a; Chakraborti et al. 2015). Several SNe in our sample, including SN 2012ap, have been observed at early times (\sim days to a month after explosion), but only SN 2012ap showed mildly relativistic material consistent with the expectations from the cocoon model. It is the only VLASS SN for which a cocoon and off-axis relativistic jet is a viable explanation. The largely uncollimated, mildly relativistic cocoon would be responsible for the early emission. The late-time VLASS emission would be powered by the off-axis relativistic jet. In this case, SN 2012ap would represent the first evidence of a cocoon and jet system from a massive stellar explosion. Future multifrequency observations will test this scenario. Thus, with the exception of SN 2012ap, we find that the late-time VLASS emission is unlikely to be caused by relativistic jets.

3.3. Emergence of Emission from a PWN

Another candidate for the cause of late-time radio emission from SNe is the presence of a PWN (e.g., Gaensler & Slane 2006; Slane 2017). Core-collapse SNe, which comprise the totality of our sample, are expected to leave a compact remnant. If a fast-rotating neutron star is left behind, it can feed a steady, highly energetic wind of relativistic particles into the SN ejecta, and this “bubble” of relativistic particles is referred to as a PWN. As this wind interacts with the slower SN ejecta, a termination shock forms, and high-energy photon emission heats and ionizes the surrounding SN ejecta. Shortly after the explosion, the emission is absorbed by the dense ejecta (e.g., Metzger et al. 2014; Murase et al. 2015, 2016, 2021). Over time, as the ejecta expands and the optical depth decreases, the PWN emission becomes observable. No SN has unambiguously shown the transition from ejecta-dominated emission to PWN-dominated emission. Recently, there have been hints toward the detection of a PWN associated with SN 1987A. This suggestion is due to nonthermal emission in the hard X-rays (Greco et al. 2021) and from the radio detection of a warm dust concentration at the center of the remnant (Cigan et al. 2019); however, alternative mechanisms to explain the emission cannot be ruled out. Beyond SN 1987A, two young SNe have been suggested to harbor PWNe (SN 1986J and SN 2012au), and both are in our VLASS SN sample.

The presence of a PWN energizing the ejecta in a young SN has been proposed to explain the anomalous state of high ionization inferred from optical spectroscopy of the H-stripped energetic SN 2012au ≈ 6 yr after explosion by Milisavljevic et al. (2018). The spectra of this transient acquired ≈ 7 yr after explosion were dominated by forbidden oxygen lines with velocities of ≈ 2300 km s^{-1} . Oxygen resides in the inner part of the SN ejecta; thus, one explanation for this emission is the presence of a pulsar that ionizes the internal material (Milisavljevic et al. 2018). The lack of narrow hydrogen in the early spectra of SN 2012au suggests a different powering mechanism than CSM–ejecta interaction and supports the scenario of ionization by a pulsar as the origin of the emission.

Bietenholz et al. (2002) suggested that the late-time radio emission from SN 1986J is evidence of a PWN. Object SN 1986J showed a broad radio spectral energy distribution (SED) 7–16 yr after explosion with a spectrum at $\nu > 10$ GHz that evolved from thin to thick (i.e., an inverted radio spectrum). However, the observed SEDs of evolved PWNe are relatively flat, with typical spectral indices between -0.3 and 0.0 . In contrast, SN 1986J has an SED that peaked at ≈ 20 GHz, with an absorbed optically thick region and an

optically thin spectral index of -0.76 . Object SN 2012au has a similarly shaped SED at 8 yr postexplosion (G. Terreran et al. 2021, in preparation). The bell-like synchrotron SEDs produced by CSM interaction of the SN shock wave peak below gigahertz frequencies on these timescales. The observed radio spectrum of SN 1986J and SN 2012au is also unusual for evolved PWNe, but we emphasize that the spectral properties of nascent PWNe that are a few years old are not observationally well constrained. From a theoretical perspective, we expect the radiative electrons to be in the “fast-cooling” regime, which can lead to radio spectra similar to those observed (e.g., Murase et al. 2016; Omand et al. 2018; Murase et al. 2021). A young PWN is expected to be smaller in size than the SN ejecta; thus, one can distinguish between the shock interaction and a PWN with very long baseline interferometry.

Interestingly, both SN 1986J and SN 2012au are in the VLASS SN sample. If the bright radio emission is confirmed to be powered by PWNe, the associated PWNe would be the two youngest discovered to date. No forming PWN has been observed in the Milky Way or the Magellanic Clouds. The youngest known galactic PWN, Kes 75, has an estimated age of 480 ± 40 yr (Reynolds et al. 2018); thus, little is known about PWN properties in the years to decades after the SN explosion.

4. Conclusions

We present evidence for a population of 19 radio-luminous SNe ($L_\nu \sim 10^{26} - 10^{29}$ erg s $^{-1}$ Hz $^{-1}$ at 3 GHz) $\approx 1 - 60$ yr after explosion found in the first epoch of the VLASS. This is part of the radio phase space of stellar explosions that has not been systematically explored so far. Our filtering procedure leveraged multiwavelength catalogs to remove potential AGN contaminants and other known radio sources, leading to a sample that is entirely comprised of core-collapse SNe and surprisingly dominated by stellar explosions with hydrogen-stripped progenitors at the time of collapse. Our main result is that the large radio luminosities at these late stages of evolution require deviation from the traditional single-wind mass-loss scenario and/or spherical shock assumption. Potential alternatives include the following.

1. Initial expansion of the SN shock into a lower-density bubble, followed by strong shock interaction with a sharp density increase (i.e., a bubble plus detached shell CSM structure). This dense shell might be connected to the shedding of the H-rich stellar envelope in the centuries before core collapse through mass-loss mechanisms that have yet to be observationally identified. VLASS SNe are as luminous as the most luminous radio SNe II in a few years postexplosion, which indicates CSM densities at large radii from the progenitors that are comparable to those inferred for SNe II.
2. While top-hat relativistic jets viewed off-axis are unlikely to provide an adequate explanation due to the underprediction of the pre-VLASS radio observations of most elements of the sample, relativistic jets with structure are not ruled out. Showing evidence for an uncollimated mildly relativistic outflow at $\delta t < 40$ days, SN 2012ap is the primary candidate for being the first jet+cocoon system in a massive star observed off-axis, which may signal that relativistic SNe are cocoons observed early on.

3. The final alternative is the emergence of a PWN. The VLASS SN sample includes SN 1986J and SN 2012au, the two young SNe that have previously been suggested to have PWN-powered late-time radio emission.

The VLA Sky Survey provides an unprecedented and unbiased window into the variable radio sky, combining the large survey area of the Northern VLA Sky Survey with the depth and angular resolution of the FIRST survey. These features, and the planned multiple field visits, are particularly useful for the discovery and study of extragalactic transients, where the angular resolution (and higher frequency, 3 GHz versus 1 GHz) minimizes confusion by the host galaxies of transients of interest. Planned interferometers such as the next-generation VLA (Carilli et al. 2015) and the Square Kilometre Array (SKA; Dewdney et al. 2009) will expand our ability to study the variable radio sky with increased depth. VLASS is complimented by other surveys and serendipitous transient discovery programs being carried out with SKA pathfinder instruments such as ASKAP (VAST; Murphy et al. 2013), Westerbork (Apertif; Adams & van Leeuwen 2019), MeerKAT (ThunderKAT; Fender et al. 2016), and LOFAR (LoTSS; Shimwell et al. 2017), which encompass a range of frequencies and angular resolutions while providing access to the southern sky.

Follow-up with multiwavelength observations, including radio SEDs and optical spectroscopy, will help constrain the mechanisms responsible for the bright radio emission of our VLASS SN sample. We will present the multiwavelength follow-up of the VLASS-detected SN sample in future papers.

We thank the referee for providing constructive comments. We also thank Seth Bruzewski for providing astrometric corrections to the VLASS quick-look epoch 1 data.

This work is supported by the Heising-Simons Foundation under grant No. 2018-0911 (PI: Margutti). R.M. acknowledges support by the NSF under grants AST-1909796 and AST-1944985. F.D.C. acknowledges support from UNAM-PAPIIT grant AG100820. R.B.D. acknowledges support from the National Science Foundation (NSF) under grant 1816694. The National Radio Astronomy Observatory is a facility of the National Science Foundation operated under cooperative agreement by Associated Universities, Inc. This publication makes use of data products from the Wide-field Infrared Survey Explorer, which is a joint project of the University of California, Los Angeles, and the Jet Propulsion Laboratory/California Institute of Technology, and NEOWISE, which is a project of the Jet Propulsion Laboratory/California Institute of Technology. WISE and NEOWISE are funded by the National Aeronautics and Space Administration. This research has made use of data obtained from the Chandra Source Catalog, provided by the Chandra X-ray Center (CXC) as part of the Chandra Data Archive. This research has made use of data obtained from the 4XMM XMM-Newton serendipitous source catalog compiled by the 10 institutes of the XMM-Newton Survey Science Centre selected by ESA. This work makes use of data supplied by the UK Swift Science Data Centre at the University of Leicester. This research was supported in part through the computational resources and staff contributions provided for the Quest high-performance computing facility at Northwestern University, which is jointly supported by the Office of the Provost, the Office for Research, and Northwestern University Information Technology. Development of

the BOXFIT code was supported in part by NASA through grant NNX10AF62G issued through the Astrophysics Theory Program and the NSF through grant AST-1009863. This research made use of APLpy, an open-source plotting package for Python (Robitaille & Bressert 2012; Robitaille 2019).

Software: APLpy (Robitaille & Bressert 2012; Robitaille 2019), Astropy (Astropy Collaboration et al. 2013, 2018), BOXFIT (van Eerten et al. 2012), Pandas (McKinney 2010), PyBDSF (Mohan & Rafferty 2015), Q3C (Koposov & Bartunov 2006), SExtractor (Bertin & Arnouts 1996).

Appendix VLASS-detected SNe

We present in Table 1 the sample of SNe detected in the VLASS data set. The second column lists whether the progenitor was hydrogen-rich or hydrogen-poor at the time of explosion. Flux densities and positions were derived as described in Section 2.5, with any deviations from the default procedure given in the “Notes” section beneath. The list of VLASS SNe is ordered by increasing R.A. Bruzewski et al. (2021) calculated the astrometric corrections required to align the VLASS quick-look epoch 1 data with the Gaia catalog, and we list the coordinates that include these astrometric corrections. The positional errors include the

uncertainties from PyBDSF fits and the astrometric corrections (S. Bruzewski, private communication) added in quadrature. We applied the corrections derived by Bruzewski et al. (2021) and astrometric uncertainties for the VLASS epoch 2.1 observations. We note that applying the VLASS epoch 1 uncertainties may overstate the positional uncertainties in the second-epoch observations, since the second VLASS epoch will have likely benefited from studying the systematic uncertainties in the first epoch (see, e.g., VLASS Memo 13¹⁸).

We report the PyBDSF flux density errors, which are purely statistical. There are known flux density offsets in the VLASS quick-look images, as detailed in VLASS Memo 13 and the CIRADA Catalogue User Guide. The detection type defines the nature of the source structure, where “S” indicates a single Gaussian that is the only source in the island, “C” indicates a single source in an island with other sources, and “M” indicates multiple Gaussian sources. The angular separation lists the distance between the listed VLASS position and the optical position. For the SN classifications, “Pec” and “BL” stand for peculiar and broad-line, respectively. Four SNe (20% of the sample) had limited follow-up, leaving the classification unknown, but they are believed to be core-collapse SNe (i.e., SN 1965G, SN 2005 ha, SDSS-II SN 8524, and SDSS-II SN 12882).

¹⁸ The VLASS Project Memo Series is listed at <https://go.nrao.edu/vlass-memos>.

Table 1
SNe Detected in VLASS Epoch 1

Name	Progenitor (H-rich/poor)	VLASS					Luminosity ($\text{erg s}^{-1} \text{Hz}^{-1}$)	Angular Separation (arcsec)	Classification
		R.A. (hh:mm:ss.ss)	Decl. (dd:mm:ss.ss)	Flux Density (mJy)	Detection (S, M, or C)	Obs. Date (MJD)			
SN 1986J	?	02:22:31.293(15)	+42:19:57.5(3)	1.3 ± 0.2	C	58,588	$(1.6 \pm 0.2) \times 10^{26}$	0.56	IIn
SN 2017hcb	H-poor	02:36:23.756(14)	+31:42:36.2(3)	0.5 ± 0.2	M	58,569	$(3.0 \pm 1.2) \times 10^{27}$	0.99	Ib
SDSS-II SN 12882	?	03:03:49.977(9)	-00:12:14.3(3)	1.7 ± 0.4^a	S	58,103	$(2.8 \pm 0.7) \times 10^{28}$	0.32	?
		03:03:49.975(10)	-00:12:14.2(3)	1.6 ± 0.3^a	S	59,078	$(2.6 \pm 0.5) \times 10^{28}$	0.41	
SN 2003bg	H-poor	04:10:59.436(6)	-31:24:50.2(3)	4.1 ± 0.2	S	58,663	$(2.83 \pm 0.14) \times 10^{27}$	0.61	IcPecBL
SN 2012at	H-poor	04:54:52.783(7)	-37:19:16.9(3)	2.0 ± 0.2	S	58,153	$(2.5 \pm 0.2) \times 10^{27}$	0.41	Ic
		04:54:52.786(8)	-37:19:17.4(3)	1.9 ± 0.2	S	59,155	$(2.3 \pm 0.2) \times 10^{27}$	0.70	
SN 2012ap	H-poor	05:00:13.734(5)	-03:20:51.4(3)	4.0 ± 0.3	S	58,027	$(8.9 \pm 0.7) \times 10^{27}$	0.25	IcBL
		05:00:13.738(5)	-03:20:51.6(3)	4.5 ± 0.3	S	59,078	$(1.00 \pm 0.07) \times 10^{28}$	0.23	
SN 2005 ha	?	06:21:49.110(6)	+00:21:56.2(3)	2.2 ± 0.2	S	58,123	$(3.7 \pm 0.3) \times 10^{27}$	1.23	?
		06:21:49.106(6)	+00:21:56.0(3)	1.9 ± 0.3	S	59,048	$(3.2 \pm 0.5) \times 10^{27}$	1.09	
SN 2002hi	H-rich	07:19:54.127(9)	+17:58:18.5(3)	2.1 ± 0.3	S	58,572	$(1.7 \pm 0.2) \times 10^{29}$	0.72	IIn
SN 2017iuk	H-poor	11:09:39.519(5)	-12:35:18.5(3)	4.8 ± 0.2	S	58,150	$(1.39 \pm 0.06) \times 10^{29}$	0.24	IcBL
		<0.45	...	59,133	$<1.3 \times 10^{28}$...	
SN 2004C	H-poor	11:27:29.80(2)	+56:52:47.9(3)	4.2 ± 0.6^b	S	58,020	$(2.8 \pm 0.4) \times 10^{27}$	0.57	Ic
		11:27:29.77(2)	+56:52:47.9(3)	5.3 ± 0.9	S	59,064	$(3.5 \pm 0.6) \times 10^{27}$	0.79	
SN 1965G	?	12:11:54.049(5)	+24:06:58.5(3)	7.7 ± 0.4	S	58,082	$(1.15 \pm 0.06) \times 10^{28}$	2.59	?
		12:11:54.045(5)	+24:06:58.4(3)	7.8 ± 0.3	S	59,099	$(1.17 \pm 0.05) \times 10^{28}$	2.52	
SN 2012cc	H-rich	12:26:56.829(9)	+15:02:45.6(3)	2.3 ± 0.4	S	58,590	$(1.10 \pm 0.19) \times 10^{27}$	0.36	II
SN 2012au	H-poor	12:54:52.257(5)	-10:14:50.5(3)	4.5 ± 0.3	S	58,553	$(3.0 \pm 0.2) \times 10^{27}$	1.16	Ib
PTF 11qej	H-poor	13:13:41.480(9)	+47:17:56.8(3)	6.8 ± 0.2	S	58,561	$(1.12 \pm 0.03) \times 10^{29}$	0.44	IcBL
SN 2009fi	H-rich	14:06:05.757(6)	+11:47:13.6(3)	2.2 ± 0.2	S	58,611	$(1.17 \pm 0.11) \times 10^{28}$	0.88	Ib
SN 2004dk	H-poor	16:21:48.872(4)	-02:16:17.6(3)	6.3 ± 0.2	S	58,624	$(3.34 \pm 0.11) \times 10^{27}$	0.75	Ib
SDSS-II SN 8524	?	21:29:23.354(6)	+00:56:42.9(3)	1.7 ± 0.2	S	58,023	... ^c	1.18	?
		<0.5	...	59,049	... ^c	...	
SN 2016coi	H-poor	21:59:04.127(8)	+18:11:10.8(3)	1.8 ± 0.2	S	58,604	$(4.7 \pm 0.5) \times 10^{26}$	0.35	IcBL
SN 2014C	H-poor	22:37:05.601(6)	+34:24:31.5(3)	29.0 ± 0.3	S	58,642	$(7.91 \pm 0.08) \times 10^{27}$	0.49	Ib ^d

Notes.



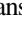


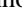







^a The region surrounding SDSS-II SN 12882 is contaminated by radial artifacts from quasar PB 6989, so the flux density could be less reliable.

^b The region surrounding SN 2004C is contaminated by radial artifacts from NVSS J112731+565240, so the flux density could be less reliable. Object SN 2004C is clearly part of an extended emission complex, which is not detected with $P_{\gamma\text{BDSF}}$ unless the island and detection threshold are both lowered. There is a clear point source at the location of SN 2004C that we associate with the transient, but the flux density here is likely unreliable.

^c Object SDSS-II SN 8524 has no known redshift; thus, a luminosity cannot be calculated.

^d Object SN 2014C was initially classified as Type Ib but later classified as Type IIn.

ORCID iDs

Michael C. Stroh  <https://orcid.org/0000-0002-3019-4577>
 Giacomo Terreran  <https://orcid.org/0000-0003-0794-5982>
 Deanne L. Coppejans  <https://orcid.org/0000-0001-5126-6237>
 Joe S. Bright  <https://orcid.org/0000-0002-7735-5796>
 Raffaella Margutti  <https://orcid.org/0000-0003-4768-7586>
 Michael F. Bietenholz  <https://orcid.org/0000-0002-0592-4152>
 Fabio De Colle  <https://orcid.org/0000-0002-3137-4633>
 Lindsay DeMarchi  <https://orcid.org/0000-0003-4587-2366>
 Rodolfo Barniol Duran  <https://orcid.org/0000-0002-5565-4824>
 Danny Milisavljevic  <https://orcid.org/0000-0002-0763-3885>
 Kohta Murase  <https://orcid.org/0000-0002-5358-5642>
 Kerry Paterson  <https://orcid.org/0000-0001-8340-3486>
 Wendy L. Williams  <https://orcid.org/0000-0001-7315-1596>

References

- Adams, E. A. K., & van Leeuwen, J. 2019, *NatAs*, 3, 188
 Assef, R. J., Stern, D., Noirod, G., et al. 2018, *ApJS*, 234, 23
 Astropy Collaboration, Price-Whelan, A. M., SipHocz, B. M., et al. 2018, *AJ*, 156, 123
 Astropy Collaboration, Robitaille, T. P., Tollerud, E. J., et al. 2013, *A&A*, 558, A33
 Balasubramanian, A., Corsi, A., Polisensky, E., Clarke, T. E., & Kassim, N. E. 2021, *ApJ*, 923, 32
 Becker, R. H., White, R. L., & Helfand, D. J. 1995, *ApJ*, 450, 559
 Bertin, E., & Arnouts, S. 1996, *A&AS*, 117, 393
 Bietenholz, M. F., & Bartel, N. 2017, *ApJ*, 851, 7
 Bietenholz, M. F., Bartel, N., Argo, M., et al. 2021, *ApJ*, 908, 75
 Bietenholz, M. F., Bartel, N., & Rupen, M. P. 2002, *ApJ*, 581, 1132
 Bietenholz, M. F., De Colle, F., Granot, J., Bartel, N., & Soderberg, A. M. 2014, *MNRAS*, 440, 821
 Brethauer, D., Margutti, R., Milisavljevic, D., & Bietenholz, M. 2020, *RNAAS*, 4, 235
 Bruzewski, S., Schinzel, F. K., Taylor, G. B., & Petrov, L. 2021, *ApJ*, 914, 42
 Carilli, C. L., McKinnon, M., Ott, J., et al. 2015, arXiv:1510.06438
 Chakraborti, S., Soderberg, A., Chomiuk, L., et al. 2015, *ApJ*, 805, 187
 Chandra, P., & Frail, D. A. 2012, *ApJ*, 746, 156
 Chevalier, R. A. 1982, *ApJ*, 259, 302
 Chevalier, R. A. 1998, *ApJ*, 499, 810
 Chevalier, R. A., & Fransson, C. 2006, *ApJ*, 651, 381
 Chevalier, R. A., & Fransson, C. 2017, in *Handbook of Supernovae*, ed. A. W. Alsabti & P. Murdin (Cham: Springer), 855
 Chomiuk, L., Soderberg, A. M., Chevalier, R. A., et al. 2016, *ApJ*, 821, 119
 Cigan, P., Matsuura, M., Gomez, H. L., et al. 2019, *ApJ*, 886, 51
 Condon, J. J., Cotton, W. D., Greisen, E. W., et al. 1998, *AJ*, 115, 1693
 Corsi, A., & Lazzati, D. 2021, *NewAR*, 92, 101614
 Corsi, A., Ofek, E. O., Gal-Yam, A., et al. 2014, *ApJ*, 782, 42
 Corsi, A., Gal-Yam, A., Kulkarni, S. R., et al. 2016, *ApJ*, 830, 42
 Cutri, R. M., Wright, E. L., Conrow, T., et al. 2013, *yCat*, 2328, 0
 D'Abrusco, R., Massaro, F., Paggi, A., et al. 2013, *ApJS*, 206, 12
 De Colle, F., Kumar, P., & Aguilera-Dena, D. R. 2018, *ApJ*, 863, 32
 De Colle, F., Kumar, P., & Hoefflich, P. 2021, arXiv:2105.09376
 de Ugarte Postigo, A., Izzo, L., & Kann, D. A. 2017, *Transient Name Server Classification Report no. 2017-1387*, 1
 Dewdney, P. E., Hall, P. J., Schilizzi, R. T., & Lazio, T. J. L. W. 2009, *IEEEP*, 97, 1482
 Evans, I. N., Primini, F. A., Miller, J. B., et al. 2020a, *AAS Meeting*, 52, 1
 Evans, P. A., Page, K. L., Osborne, J. P., et al. 2020b, *ApJS*, 247, 54
 Fender, R., Woudt, P. A., Corbel, S., et al. 2016, in *Proc. of MeerKAT Science: On the Pathway to the SKA (Trieste: SISSA)*, 13
 Gaensler, B. M., & Slane, P. O. 2006, *ARA&A*, 44, 17
 Gordon, Y. A., Boyce, M. M., O'Dea, C. P., et al. 2020, *RNAAS*, 4, 175
 Granot, J., De Colle, F., & Ramirez-Ruiz, E. 2018, *MNRAS*, 481, 2711
 Granot, J., Panaitescu, A., Kumar, P., & Woosley, S. E. 2002, *ApJL*, 570, L61
 Greco, E., Miceli, M., Orlando, S., et al. 2021, *ApJL*, 908, L45
 Hallinan, G., Mooley, K., Dong, D., et al. 2020, *ATel*, 14020, 1
 Izzo, L., de Ugarte Postigo, A., Maeda, K., et al. 2019, *Natur*, 565, 324
 Kamble, A., Soderberg, A. M., Chomiuk, L., et al. 2014, *ApJ*, 797, 2
 Kposov, S., & Bartunov, O. 2006, in *ASP Conf. Ser. 351, Astronomical Data Analysis Software and Systems XV*, ed. C. Gabriel et al. (San Francisco, CA: ASP), 735
 Lacy, M., Baum, S. A., Chandler, C. J., et al. 2020, *PASP*, 132, 035001
 Lazzati, D., & Begelman, M. C. 2005, *ApJ*, 629, 903
 Lazzati, D., Morsony, B. J., Blackwell, C. H., & Begelman, M. C. 2012, *ApJ*, 750, 68
 Margutti, R., & Chornock, R. 2021, *ARA&A*, 59, 43
 Margutti, R., Kamble, A., Milisavljevic, D., et al. 2017, *ApJ*, 835, 140
 Margutti, R., Milisavljevic, D., Soderberg, A. M., et al. 2014a, *ApJ*, 797, 107
 Margutti, R., Milisavljevic, D., Soderberg, A. M., et al. 2014b, *ApJ*, 780, 21
 Marsden, B. G. 2005, *CBET*, 260, 4
 Matzner, C. D., & McKee, C. F. 1999, *ApJ*, 510, 379
 Mazzali, P. A., Valenti, S., Della Valle, M., et al. 2008, *Sci*, 321, 1185
 Metzger, B. D., Vurm, I., Hascoët, R., & Beloborodov, A. M. 2014, *MNRAS*, 437, 703
 Milisavljevic, D., Patnaude, D. J., Chevalier, R. A., et al. 2018, *ApJL*, 864, L36
 Milisavljevic, D., Margutti, R., Crabtree, K. N., et al. 2014, *ApJL*, 782, L5
 Milisavljevic, D., Margutti, R., Kamble, A., et al. 2015b, *ApJ*, 815, 120
 Milisavljevic, D., Margutti, R., Parrent, J. T., et al. 2015a, *ApJ*, 799, 51
 Mohan, N., & Rafferty, D. 2015, *PyBDSF: Python Blob Detection and Source Finder*, Astrophysics Source Code Library, ascl:1502.007
 Morsony, B. J., Lazzati, D., & Begelman, M. C. 2007, *ApJ*, 665, 569
 Murase, K., Franckowiak, A., Maeda, K., Margutti, R., & Beacom, J. F. 2019, *ApJ*, 874, 80
 Murase, K., Kashiyama, K., Kiuchi, K., & Bartos, I. 2015, *ApJ*, 805, 82
 Murase, K., Kashiyama, K., & Mészáros, P. 2016, *MNRAS*, 461, 1498
 Murase, K., Omand, C. M. B., Coppejans, D. L., et al. 2021, *MNRAS*, 508, 44
 Murphy, T., Chatterjee, S., Kaplan, D. L., et al. 2013, *PASA*, 30, e006
 Nakar, E. 2020, *PhR*, 886, 1
 Nakar, E., & Piran, T. 2017, *ApJ*, 834, 28
 Omand, C. M. B., Kashiyama, K., & Murase, K. 2018, *MNRAS*, 474, 573
 Palliyaguru, N. T., Corsi, A., Frail, D. A., et al. 2019, *ApJ*, 872, 201
 Pooley, D., Wheeler, J. C., Vinkó, J., et al. 2019, *ApJ*, 883, 120
 Reynolds, S. P., Borkowski, K. J., & Gwynne, P. H. 2018, *ApJ*, 856, 133
 Rhoads, J. E. 1997, *ApJL*, 487, L1
 Robitaille, T. 2019, *APLpy v2.0: The Astronomical Plotting Library in Python*, Zenodo, doi:10.5281/zenodo.2567476
 Robitaille, T., & Bressert, E. 2012, *APLpy: Astronomical Plotting Library in Python*, Astrophysics Source Code Library, ascl:1208.017
 Sari, R., Piran, T., & Halpern, J. P. 1999, *ApJL*, 519, L17
 Shimwell, T. W., Röttgering, H. J. A., Best, P. N., et al. 2017, *A&A*, 598, A104
 Shimwell, T. W., Tasse, C., Hardcastle, M. J., et al. 2019, *A&A*, 622, A1
 Slane, P. 2017, in *Handbook of Supernovae*, ed. A. W. Alsabti & P. Murdin (Cham: Springer), 2159
 Smith, N. 2014, *ARA&A*, 52, 487
 Soderberg, A. M., Chevalier, R. A., Kulkarni, S. R., & Frail, D. A. 2006a, *ApJ*, 651, 1005
 Soderberg, A. M., Chakraborti, S., Pignata, G., et al. 2010, *Natur*, 463, 513
 Soderberg, A. M., Margutti, R., Zauderer, B. A., et al. 2012, *ApJ*, 752, 78
 Soderberg, A. M., Kulkarni, S. R., Berger, E., et al. 2005, *ApJ*, 621, 908
 Soderberg, A. M., Nakar, E., Berger, E., & Kulkarni, S. R. 2006b, *ApJ*, 638, 930
 Terreran, G., Margutti, R., Bersier, D., et al. 2019, *ApJ*, 883, 147
 van Eerten, H., van der Horst, A., & MacFadyen, A. 2012, *ApJ*, 749, 44
 Webb, N. A., Coriat, M., Traulsen, I., et al. 2020, *A&A*, 641, A136
 Wellons, S., Soderberg, A. M., & Chevalier, R. A. 2012, *ApJ*, 752, 17
 McKinney, W. 2010, *Proc. of the 9th Python in Science Conference*, *Data Structures for Statistical Computing in Python*, ed. S. van der Walt & J. Millman, 56, <http://conference.scipy.org/proceedings/scipy2010/pdfs/mckinney.pdf>
 Williams, W. L., Hardcastle, M. J., Best, P. N., et al. 2019, *A&A*, 622, A2
 Wright, E. L., Eisenhardt, P. R. M., Mainzer, A. K., et al. 2010, *AJ*, 140, 1868
 Wu, S., & Fuller, J. 2021, *ApJ*, 906, 3
 Xu, C. Y., & Wei, D. M. 2008, *AcASn*, 49, 387
 Zhao, X., & Fuller, J. 2020, *MNRAS*, 495, 249